Coastal REsearch and Transportation Education
Tier 1 University Transportation Center
U.S. Department of Transportation

SEAHIVE® solutions to mitigate bridge scour – Phase I
Part 1
June 29, 2024

Nanni, Antonio, Ph.D., P.E., Professor at University of Miami, Department of Civil & Architectural Engineering, 1251 Memorial Drive, McArthur Engineering Building, FL 33146; ORCID https://orcid.org/0000-0003-2678-9268; Email: nanni@miami.edu
Barbarigos, Landolf, Ph.D., Associate Professor at University of Miami, 1251 Memorial Drive, McArthur Engineering Building, FL 33146; ORCID https://orcid.org/0000-0001-7550-800X; Email: landolfrb@miami.edu

Kulesza, Stacey, Ph.D., P.E., Associate Professor at Texas State University, Ingram School of Engineering, 327 W Woods St, San Marcos, TX 78666; ORCID https://orcid.org/0000-0000-0000-0000; Email: sekulesza@txstate.edu

Mirdarsoltany, Mohammadamin, Ph.D. Student at University of Miami, Department of Civil & Architectural Engineering, 1251 Memorial Drive, McArthur Engineering Building, FL 33146 Email: mxm193871@miami.edu

Annual Research Report – Part 1

Prepared for:

Coastal REsearch and Transportation Education

ACKNOWLEDGMENT

This study was funded, partially or entirely, by the U.S. Department of Transportation through the Coastal REsearch And Transportation Education University Transportation Center under Grant Award Number 69A3552348330. The work was conducted at the University of Miami.

DISCLAIMER

ABSTRACT

Protecting coastal regions is crucial because of high population density and important economic significance. Numerous strategies have been suggested to safeguard coastal regions and bridge piers from scouring, encompassing natural and man-made approaches. Given the constraints of existing techniques, this study examines a new method named SEAHIVE®, which is designed to improve the performance of engineered structures. This method incorporates hexagonal, hollow, and perforated concrete elements, which are reinforced with glass fiber-reinforced polymer (GFRP) bars or wraps. To investigate the load-bearing capacity, SEAHIVE® specimens were tested under pure compression (cut-off samples) and flexure (full samples). For specimens under pure compression, analysis, and experimentation showed that cracks started due to exceeding the concrete tensile strength in the inclined leg of the hexagon and eventually led to failure in both elements reinforced with GFRP bars or wraps. In elements reinforced with GFRP bars tested under flexure, the strut-and-tie analysis confirmed that SEAHIVE® beam-like specimens failed because of inadequate development length of longitudinal bars and toe crushing. As for the sample reinforced with GFRP wraps under flexure, cracks initiated due to the slipping and loss of the longitudinal GFRP strips.

Keywords: GFRP Reinforcement; Reinforced Concrete; Flexure; Compression; Shear; Hollow Concrete Shape.

Table of Contents

List of Figures

List of Tables

INTRODUCTION

Around 40% of the populace resides close to the coast, while the Southeast United States hosts more than 70 million individuals and encompasses 29,000 miles of coastline[1]. Such areas are susceptible to hurricanes and winds, leading to bigger waves and storm surges. In addition to physical and mental disturbances, these natural hazards are responsible for economic losses [2–4]. Prominent instances like Hurricanes Ian and Michael underscore the ongoing significant need to explore effective and cos-efficient measures that decrease the impact and risk to the Southeast United States. As per a recent report by the National Centers for Environmental Information, since 1980, weather and climate disasters cost $2 trillion in the United States [5]. These events include tropical cyclones and hurricanes, which bring extreme winds, rain, storm surge, and waves to coastal communities with often devastating impacts. In the last ten years alone, tropical cyclones and hurricanes are responsible for more than 53% of the total damages/costs and more than 6,500 deaths. Considering that 29% of the total U.S. population lives near the coast, identifying sustainable solutions against hazards, such as flooding and wave attacks, represents a critical societal need.

There has been research to protect shorelines by hard solutions, such as seawalls or breakwaters [6,7]. However, conventional seawalls are ineffective in terms of dissipating wave energy. Also, reflected waves have the potential to create suspended sediments, making shorelines more susceptible to erosion. The potential of seawalls to exacerbate wave energy is of concern [8]. Additionally, such measures do not provide a hospitable environment for biodiversity; seawalls typically support 23% lower biodiversity and 45% fewer organisms than natural shorelines[9]. "Living Shorelines" are often considered as the ideal ecofriendly protection barrier.

Attempts have been made to study and develop hard solutions that can provide effective, efficient, and sustainable solutions for protecting shorelines and a hospitable environment for marine creatures. Among them, Ghiasian et al. [6] developed and studied wave-energy dissipation of new hollow-hexagon RC shapes (i.e., SEAHIVE®). The proposed RC system has perforations that dissipate wave energy effectively and is found to be more eco-friendly for providing a hospitable environment for natural habitats in protected coastlines with this system [8].

Apart from the application of SEAHIVE® in coastal protection and dissipating wave energy, this technology has the potential to be used as a countermeasure to prevent scouring in bridge piers, retaining walls, and bulkheads riverbeds. The predominant factors for bridge collapse are attributed to hydraulic causes, such as scour, floods, stream instability, lateral migration, and floating debris [10,11]. Among the mentioned factors, scour is to blame as the most frequent culprit, accounting for about 66% of bridge collapses in North America and Europe [10]. The available data for the United States showed that 20% of bridge collapses are attributed to scour [1,12–14]. Different types of scours influence the bridges in the erosion process. They are divided into three main categories, namely local scour, general scour, and contraction scour, acting independently or in combination with other hydraulic agents to cause a collapse in the bridge [15].

The mechanism of local scouring is in a way that the bridge piers impede the flow stream, and this causes large-scale turbulence structures. This turbulence not only exacerbates the turbulence in the flow-down-ward towards the bed which is called horseshoe vortex, but also increases the turbulence behind the bridge pier which is called the wake vortex [16]. It can be concluded that the main root of local scouring is attributed to the hydraulic structures interfering by obstructing the natural flow field [17]. When it comes to general scour, it can be categorized as either prolonged or short-term erosion. The root of this mechanism involves removing the sediments from the bed river and bank river from the width of the channel [18]. As opposed to the local and contraction scour, the bridge pier is not a factor in causing this mechanism. As for the contraction scour, this is attributed to the acceleration of the flow due to the obstruction and contraction, such as a bridge. This type of scouring is narrowed down to the length of contraction [18,19]. To protect the bridge piers from scouring incorporating SEAHIVE® technology is proposed. The presence of perforations on the surfaces of hollow hexagons holds the potential to alter hydraulic flow dynamics in areas surrounding a pile cap, as well as within the interstices between piles, where contraction and local scour may occur [6].

Figure 1 Local scouring a bridge pier after flow event.

Although the energy dissipation of SEAHIVE® is well-studied, there is a need to evaluate structural performance including the effects of different fabrication methods of these units. Based on available literature, some information can be drawn from research conducted on the flexural behavior of solid cross-section beams with openings on their sides. Researchers [20–22] have proposed design guidelines to assist in determining the appropriate sizes and placements of web openings. Additionally, Tan and Mansur [23] provided design guidelines for RC beams with large web openings, considering both ultimate and serviceability limit states. Daniel and Revathy [24] showed that beams with rectangular openings exhibit significantly reduced ultimate flexural resistance and stiffness compared to solid beams. Al-Sheikh [25] investigated the flexural behavior of RC beams with circular, square, and rectangular openings, concluding that beams with a single circular opening performed best, with ultimate capacity reductions of about 1.5% for small openings and 10% for large openings. Aykac and Yilmaz [26] determined that circular openings are more effective than triangular openings in terms of ductile behavior. Moreover, it was found that introducing large openings without adequate internal reinforcement could significantly reduce ultimate capacity [20]. However, providing sufficient diagonal reinforcement around the openings prevented the shear failure of the web posts and premature failure of the beam [27]. Despite the mentioned research on the flexural performance of the perforated solid-cross section of the beams, there is a lack of data on the performance of the perforated hollow units with a hexagonal cross-section.

When it comes to the fabrication method of SEAHIVE® units, they can currently be carried out by at least three different methods, namely: wet-cast, dry-cast, and 3D printed methods. Dry-cast concrete consists of using zero slump concrete (See Figure 2 (a)) which is formed with various methods and immediately removed from its forming setup and let to cure. The very first dry-cast product was concrete blocks and concrete pipes at the very beginning of 1900s (See Figure 2(b)), with the method extending to structural applications like T-joists (See Figure 2(c)) in the 1930s and prestressed concrete hollow-core slabs in the 1950s (See Figure 2(d)).

(a)

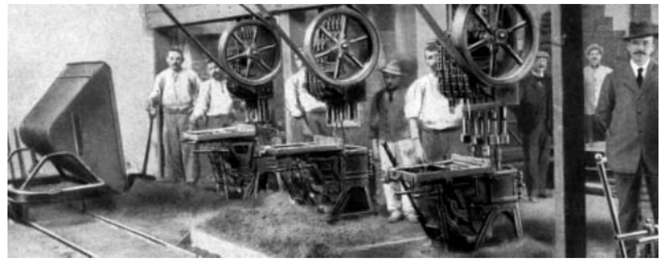

(b)

(c)

(d)

Figure 2 (a) Zero slump concrete; (b) Concrete block production in the early 1900s; (c) Production of T-joust in the 1930s; (d) Prestressed hollow-core slabs in the 1950s

The dry-cast method is normally used for high-volume production since it requires a high capital investment, but it permits much higher productivity compared with traditional wet-cast processes (wet-cast products are manufactured using fluid concrete that is poured into forms for shaping and curing). Another significant advantage of the dry-cast with an immediate stripping process is in the product strength. This happens for two main reasons, the first is because the water-to-binder (w/c) ratio of the concrete never exceeds 0.4 (most common is 0.3) for process reasons, and the second is because the packing action is normally one order of magnitude higher than what obtainable with traditional wet-cast concrete.

When it comes to reinforcing SEAHIVE®, using conventional materials such as black steel bars are not a sustainable solution due to the vulnerability of steel to corrosion. For example, the portion of the seawalls exposed to tides and waves becomes a weaker link reducing their service life. As an alternative, SEAHIVE® can be reinforced by either external GFRP wraps or internal GFRP bars (See Figure 3) [8,28–34].

Because of the expenses related to providing equipment for fabricating elements with the dry-cast method, this research is initially focused on evaluating the structural performance of wet-cast SEAHIVE® reinforced externally with GFRP wraps or internally with FRP stirrups and longitudinal reinforcement.

(a)

(b)

Figure 3 (a) SEAHIVE® with internal reinforcements (b) SEAHIVE® with external reinforcement

UNITS REINFORCED INTERNALLY WITH GFRP BARS

Test Specimens

To investigate the capacity of SEAHIVE®, four specimens were tested: two under pure compression and two under flexure, respectively. To investigate the capacity of SEAHIVE®, four specimens were tested to study structural performance: two under longitudinal compression and two under flexure, respectively. The configuration and preparation of each specimen are summarized in Table 1 and depicted in Figure 4..

Table 1 Configuration of SEAHIVE® samples

Specimen ID	**D/t***	**Loading type**	**Specimen Length (mm)**	**Objectives**
CB-1	0.25	Monotonic quasi-static pure compression	910	Study the effect of pure compression
CB-2	0.25	Cyclic quasi-static pure compression	910	
FB-1	0.25	Monotonic quasi-static flexure	1830	Study the effect of four-point bending
FB-2	0.25	Cyclic quasi-static flexure	1830	

notes D/t *= side perforation diameter to total height of the unit

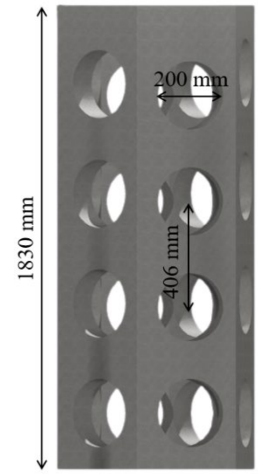

(a)

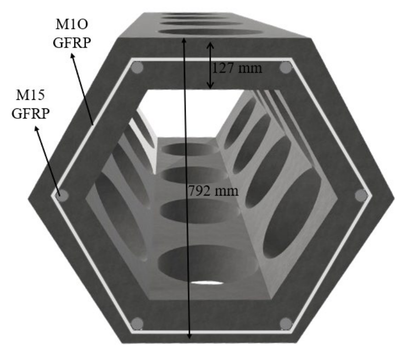

(b)

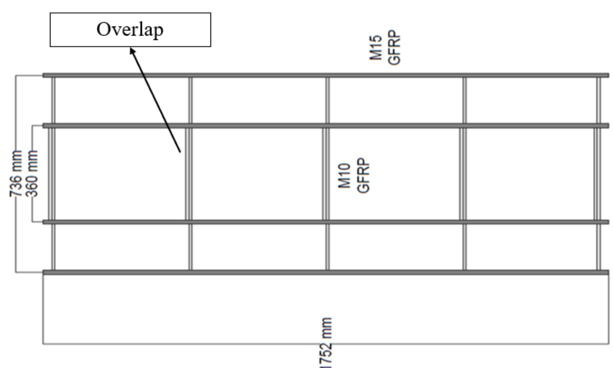

(c)

Figure 4 The geometry of the SEAHIVE® unit with reinforcement details

The total length of the unit for the flexural test was equal to 1.83 m (see Figure 4(a)), a dimension that corresponds to production specifications. For the compression test, specimens were obtained by saw-cutting a unit into two parts to have two elements with 0.91 m length each. The diameter of the holes on the surface of the hexagon was equal to 200 mm, provided at 406 mm center to center (see Figure 4(a)). The length and thickness of each leg of the GFRP-RC hexagon was 280 and 127 mm, respectively, and the overall depth of the cross-section was equal to 792 mm (See Figure 4(b)). The SEAHIVE® elements were reinforced with 6-M15 GFRP longitudinal bars provided at corners and M10 GFRP stirrups with a spacing of 400 mm (See Figure 4(c)). As shown in Figure 4(c), the overlap provided for the initial and last legs of each stirrup was 360 mm [35].

Materials

GFRP characterization

Data on the mechanical performance of GFRP bars M10 and M15 were obtained experimentally. The tensile properties of the GFRP bars were determined following the provisions of ASTM D7205 [36]. For each type of bar, three specimens were cut to a length of 1270 mm. ASTM D7205 requires rigid pipe-shaped anchors at both ends of the bar as an interface layer between the grip and the FRP bar; therefore, steel pipes having an outer diameter of 42 mm, a thickness of 5.08 mm, and a length of 375 mm are used and filled with expansive cement grout. A vertical Universal Testing Machine (UTM) with a maximum capacity of 2,000 kN was used to test the bars, and a 100 mm extensometer was installed in the middle of the bar to measure the tensile strain. *Table* 2 presents the properties of GFRP bars obtained from tensile tests, noting that the data as presented for M10 bars were obtained from straight pieces supplied by the manufacturer and not obtained from cutting the stirrups. The reduction in strength of GFRP bars with increasing diameter from M10 to M15 is due to the shear-lag effect.

Concrete Characterization

Six cores from two different SEAHIVE® units were extracted to obtain the concrete compressive strength used in fabrication. The diameter of the extracted cores was 50.8 mm, and the height after trimming the ends was 101.6 mm. Based on ASTM C39, cores were tested under compression [37]. Before testing, both core ends were sulfur-capped to have planar and parallel surfaces (See Figure 5). The average compressive strength of the concrete cores was 40 MPa with a standard deviation of 2.6. The concrete mix constituents and proportions were not provided by the manufacturer. By inspection, it was observed that the maximum aggregate size was 25 mm corresponding to half the diameter of the core. Ergun and co-workers [38] showed that the compressive strength of the concrete cores drilled perpendicular to the direction of casting with length to diameter ratio of two is 83% of the 28-day compressive strength of the standard cylinder concrete specimens. However, the compressive strength of 40 MPa was used in the analysis.

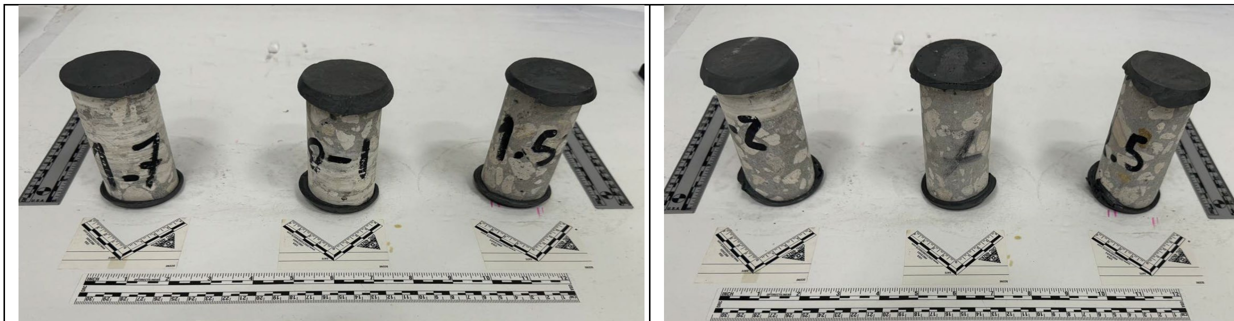

Figure 5 Concrete cores extracted from two different units

Table 2 Material properties of concrete and GFRP bars

Designation	Elastic modulus (MPa)	Ultimate tensile strength (f_{fu})(MPa)	Ultimate strain	Concrete strength (MPa)	Concrete clear cover (mm)
M15	60,790	991	0.0163	-	63.5
M10	61,600	1274	0.021	-	58.5
Concrete	24,870*	-	0.003**	40.0	-

Notes: *= value derived from code provisions; **=design value from code

Test Set-up and Instrumentation

Half Unit under Pure Compression

The experimental setup for the compressive test is shown in Figure 6 for specimens 0.91 m in length. To ensure that the applied load from the two hydraulic jacks was distributed uniformly across the element's surface, two 914 x 457 mm^2 masonite sheets were used on the surface of the element followed by two 305 x 406 mm^2 steel plates. Thereafter, the load cells were placed over the steel plates and the load was applied by means of two hydraulic jacks operated manually.

Strain gauges were used to measure strains on the concrete surface, whereas linear variable differential transformers (LVDTs) were used to measure displacements (See Figure 7(a) and Figure 7(b)). The instruments were connected to a data logger to record the applied load, strain, and displacement values.

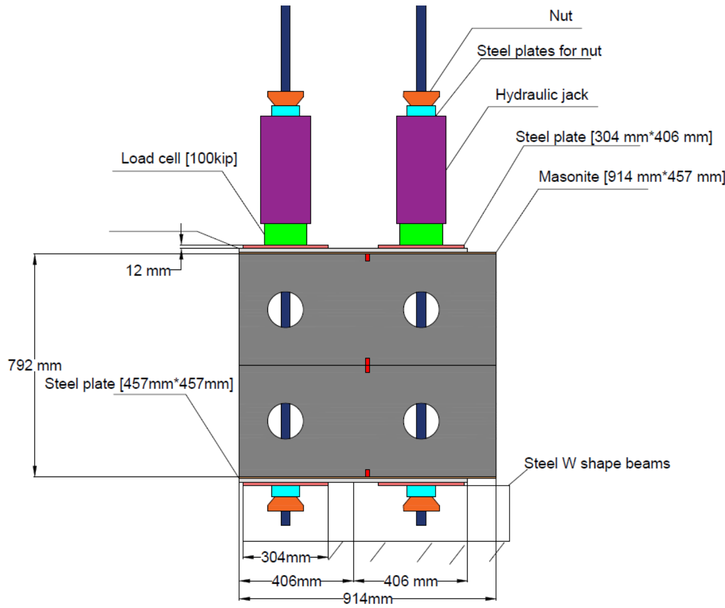

(a)

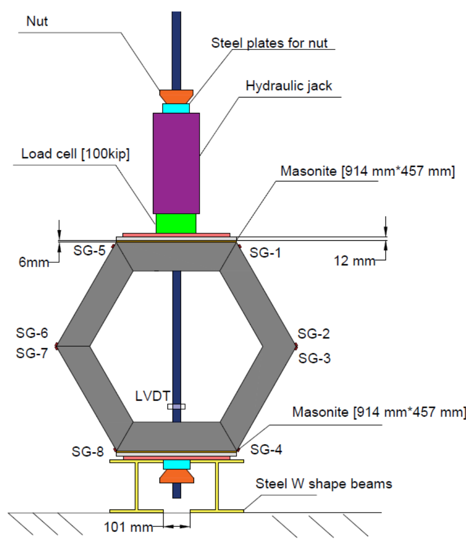

(b)

Figure 6 Sketch of compression test configuration: (a) side and (b) cross-sectional views

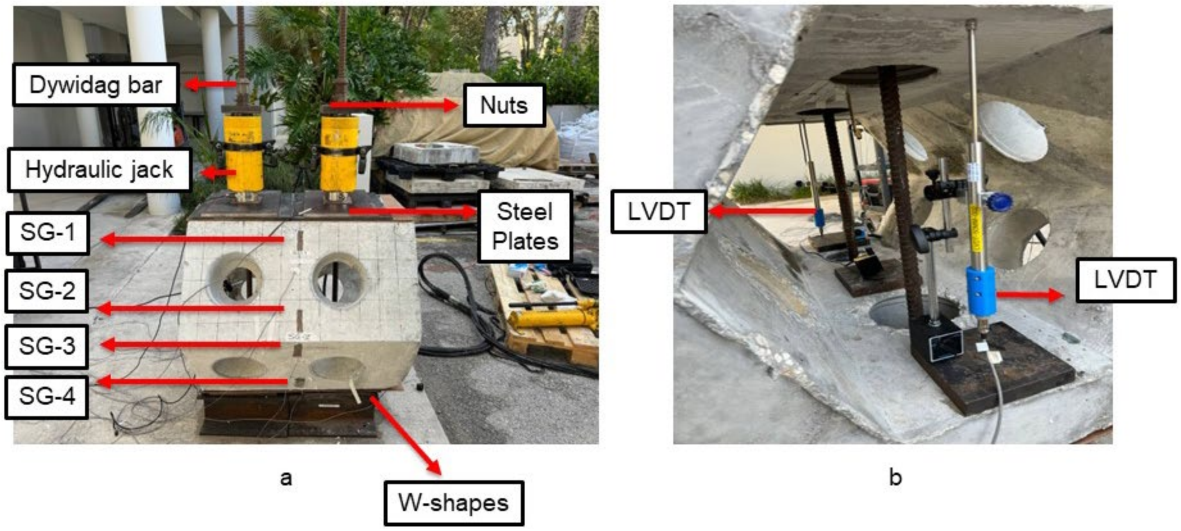

Figure 7 Location of: (a) strain gauges (b) LVDTs

Unit under Flexure

Two full-size units were tested under four-point bending to investigate the flexural behavior of the specimens. As shown in Figure 8, the distance between a support and a loading point (i.e., shear arm=a) is 635 mm, while the total height of the sample (i.e., h) is approximately 792 mm. The a/h ratio is about 0.8 (See Figure 8(a)), indicating that the unit being tested can be characterized as a deep beam. Two hydraulic jacks each located at a distance of 686 mm from the end of the specimen were used to apply the load. Masonite sheets were used below steel plates to avoid possible local concrete crushing due to surface imperfections. Strain gauges on one side of the specimen at the mid-length were positioned to measure strain at the top and bottom of the unit. These strain gauges provided valuable data on how strains were generated under the applied flexural load. Figure 9 shows LVDTs positioned mid-depth on both sides of the specimen to measure vertical displacement.

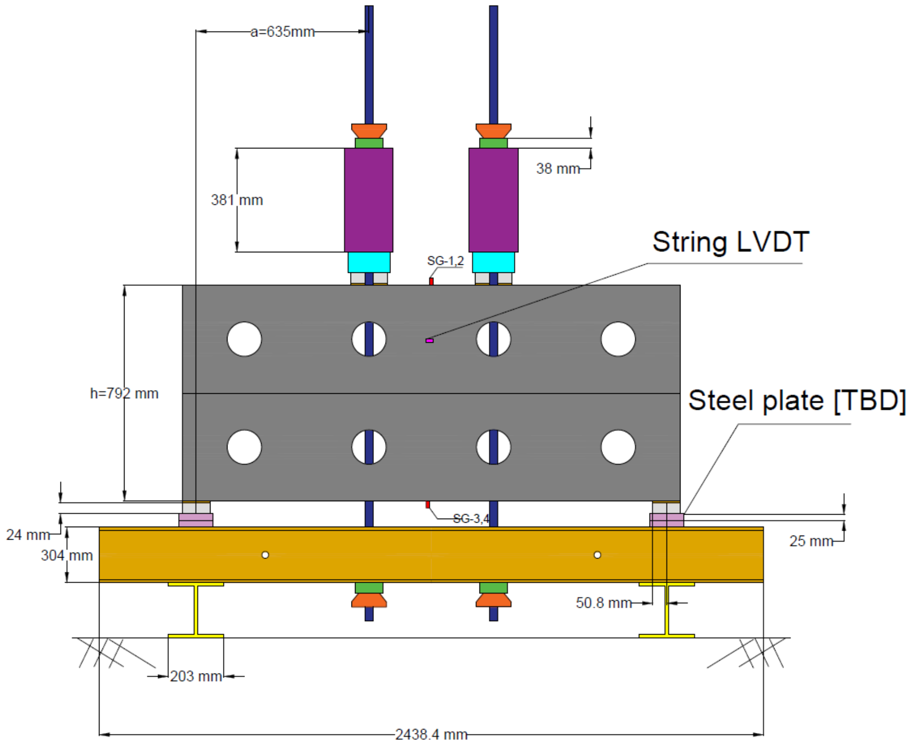

(a)

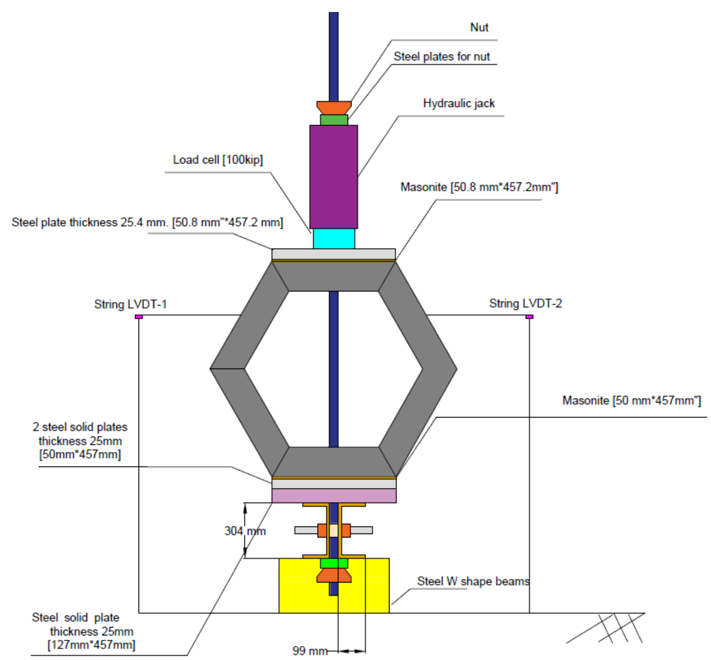

(b)

Figure 8 Sketch of the flexural test configuration: (a) side and (b) cross-sectional views

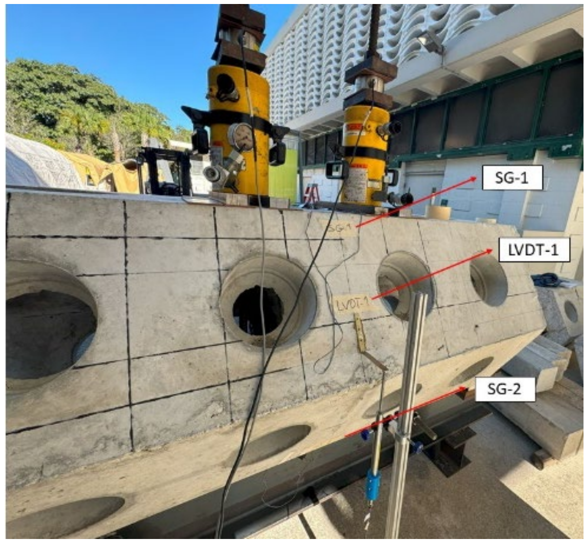

Figure 9 LVDTs on one side of the tested sample under a four-point flexural test

Loading Protocol

Quasi-static load protocols were used in both compression and four-point flexural tests. The first specimen of each test type was loaded with monotonically increasing load till failure allowing for the determination of the ultimate capacity of the element. The second specimen was loaded with progressively increasing quasi-static loading and unloading cycles to understand the crack propagation and recovery of deformation when the load was removed. Two load-unload cycles were applied to the specimens with peak loads corresponding to approximately one-third and two-thirds of the capacity determined under monotonic loading and with the third cycle till failure.

Results and Discussion

This section provides information on experimental results regarding crack patterns and load-displacement curves for both pure compression and bending tests. Moreover, data from strain gauges positioned at different locations are provided. The first cracking load, ultimate loads, and maximum displacement or mid-span deflection were recorded.

Compression Test Results

Crack Pattern and Failure Mode:

Figure 10(a) and Figure 10(b) show the CB-1 specimen during loading and at failure, respectively. It can be observed that the first crack started at the location of the holes. The crack propagated horizontally along the mid-depth of the leg of the hexagon. Inclined cracks, possibly due to shear, started after initial horizontal cracks. The failure occurred when the horizontal cracks grew in length, connecting holes in the hexagon.

A similar pattern was observed in the CB-2 specimen (See Figure 10(c) and Figure 10(d)) showing the specimen after failure and after the first loading cycle, respectively. However, in this case, together with horizontal mid-leg cracks others formed at the hexagon corners (See Figure 10(c)).

The presence of longitudinal and transverse reinforcement does not appear to contribute to the resistance capacity under this loading condition and the only function provided by the reinforcement is to prevent the specimen from falling apart after failure.

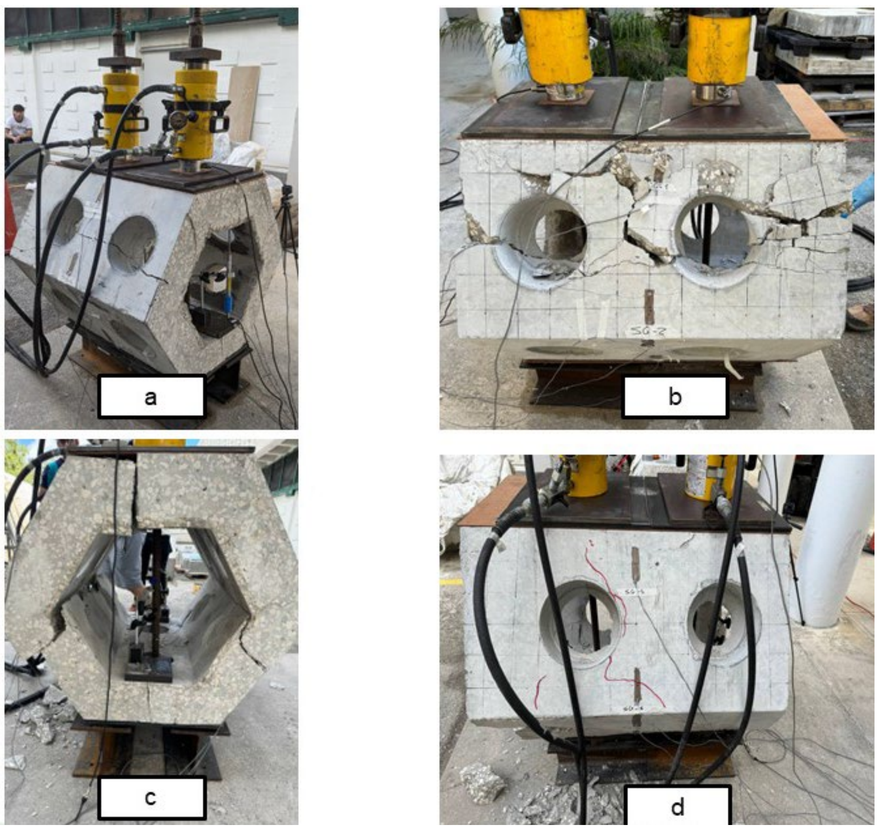

Figure 10 Cracking pattern in (a) CB-1 failure; (b) CB-1 after failure; (c) CB-2 after failure; and, (d) CB-2 at the end of the first load cycle

Load Displacement Curves:

Figure 11 shows the load-displacement diagram of CB1 and CB-2 tested under pure compression. The horizontal axis indicates the average displacement between two LVDTs, and the vertical axis shows the average applied load. The first crack occurrence is shown in the diagram by a load drop in both CB-1 and CB-2 around 73 and 79 kN, respectively. After that, the specimen continued to carry the load with a significantly reduced stiffness until failure.

Figure 11 Load-displacement results of compressive test

Strain Gauges Values:

Figure 12 shows strain gauge measurements recorded on CB-1. The values shown in the diagram are limited to what was captured by the data logger which stopped before the element failure. Because of the similarity of outcomes between CB-1 and CB-2, only data relative to CB-1 are presented. It can be observed that strain gauges positioned on the two sides of the hexagon at the same locations recorded very similar patterns, indicating a consistently symmetric behavior under load. Positive strain values in Figure 12 represent tension, whereas negative values correspond to compression. It can be observed that none of the strain gauges shows values close to cracking stress (tension) or crushing (compression) due to their location away from the critical zones.

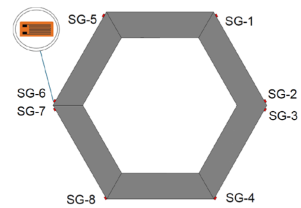

Figure 12 Measurements from eight strain gauges in CB-1

Flexure Test Results

Crack Pattern and Failure Mode:

Figure 13 shows the specimens tested under the four-point bending. Similar to specimens under pure compression, a horizontal crack formed at mid-leg between the holes. Figure 13 shows a photograph taken close to the end of the third loading cycle where it is apparent that failure was initiated by arching with a combination of crushing of the concrete toe and slipping of the longitudinal reinforcement not properly anchored.

Figure 13 Cracking pattern of FB-2 near the end of the final cycle

Load Displacement Curves:

For FB-1, strain gauges and LDVTs measurements could not be recovered due to the data logger crash. The hydraulic pressure gauge in FB-1 recorded loads at cracking and failure of about 90 and 220 kN, respectively. Figure 14 shows the load-displacement diagram of FB-2 where the horizontal axis indicates the average displacement of two LVDTs, and the vertical axis shows the total applied load (i.e., sum of two load cells). According to the experimental data, the first drop in load corresponding to first crack was recorded at 156 kN.

Figure 14 Load-displacement results of FB-2

Strain Gauge Values:

Figure 15 shows the measurements obtained by four strain gauges applied to FB-2 symmetrically on the bottom (3 and 4) and top (1 and 2) faces of the mid-span of the beam-like specimen. The first observation is that there was good symmetry in terms of load distribution. Strain gauges 1 and 2 very clearly indicate that the compressive strain at the top chord of the unit remained one order of magnitude below the crushing level. Conversely, strain gauges 3 and 4 at the bottom of the unit reached values close to the expected concrete cracking threshold, indicating that vertical cracking was reached in correspondence with the holes. Table 3 summarizes the results of the experiments on four tested specimens.

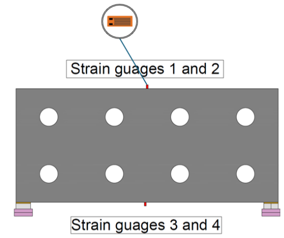

Figure 15 Results of strain gauges on FB-2

Table 3 Results of the experimental test on specimens

Load or Deflection	Specimens ID			
	CB-1	CB-2	FB-1	FB-2
First cracking load (kN)	73	79	89	156
Ultimate load (kN)	143	179	222	250
Maximum deflection (mm)	17	19	N/A	10

Analysis

Specimens under Compression

It can be observed in Figure 16 that the first cracks appeared in the middle of the inclined leg of the hexagon. The failure at this location resulted from the combined effect of axial and flexural stresses (See Figure 16). The maximum tensile stress in the leg due to the combined effect of moment and axial load was calculated using conventional analysis (i.e., $\sigma_b = -\frac{My}{I} + \frac{P}{A}$).

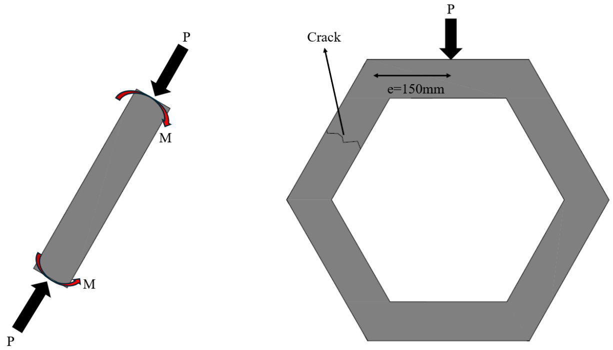

Figure 16 Combined axial force and moment resulted in the inclined leg

The effective moment of inertia was calculated by subtracting the moment of inertia of two holes from the gross cross-section moment of inertia of the leg as shown below:

$$\mathrm{I} = 86885578\ mm^4$$

The cross-sectional area equals $A = 64643\ mm^2$. The first visible cracks on the specimen appeared at a load between 73 and 79 kN, as per Table 3. Therefore, the load on each leg was equal to about 38 kN. The moment at mid-height of the leg (i.e., location of holes) was calculated by multiplying the applied load with its eccentricity (e) assumed to be 150 mm (See Figure 16). The stress at cracking was calculated as shown below:

$$\sigma_b = -\frac{38000 * 150 * 63.5}{86885578} + \frac{38000}{64643} = -3.6\ \mathrm{MPa}$$

The tensile modulus of rupture in concrete (f_r) can be calculated from Eq. (1) when the concrete compressive strength (f'_c) is equal to 40 MPa.

$$f_r = 0.62\sqrt{f_c'} = 0.62\sqrt{40} = 3.92\ \mathrm{MPa} \qquad \textbf{Eq. 1}$$

The tensile modulus of rupture in concrete was calculated is to 3.92 MPa. The maximum tensile stress due to the combined axial load and moment at the load of 78 kN (i.e., cracking load) is very close to the tensile strength (i.e., 3.6 and 3.92 MPa) thus causing the first crack that eventually caused the failure due to the insufficient transverse reinforcement. Even though the reinforcement detailing with ACI 440.11-22 [39], this Code was used to calculate the moment capacity of the section (M_n) and to compare it with the cracking moment (M_{cr}). The moment capacity and cracking moment were calculated based on sections 22.3 and 19.2.3 of ACI 440.11-

22 [39], respectively. The calculated moment capacity equals 13.025 kN.mm and the cracking moment equals 62.758 kN.mm; thus, showing that the reinforcement in the form of stirrups is totally insufficient in the case of pure compression.

Specimens under Flexure

Gohar et al. [40] concluded that when the diameter of the holes on the surface of concrete beams under bending stress exceeds 0.25 times the total depth of the beam, traditional beam theory can no longer be applied. Instead, frame action takes precedence over beam-type behavior, as depicted in Figure 17; thus, using the beam-theory method is not applicable for this condition. In this study, the hole diameter is 200 mm, and there are eight holes on each side of the unit (four holes on the top of each other) so the ratio of the diameter of the holes to the total depth of the concrete exceeds 0.25, surpassing the limit established in the referenced study. The presence of holes on all surfaces of the hexagonal, hollow, perforated specimen makes analysis complex. Moreover, the shear span-to-reinforcement depth ratio of the SEAHIVE® was equal to 0.8; therefore, conventional beam theory is not appropriate for its analysis.

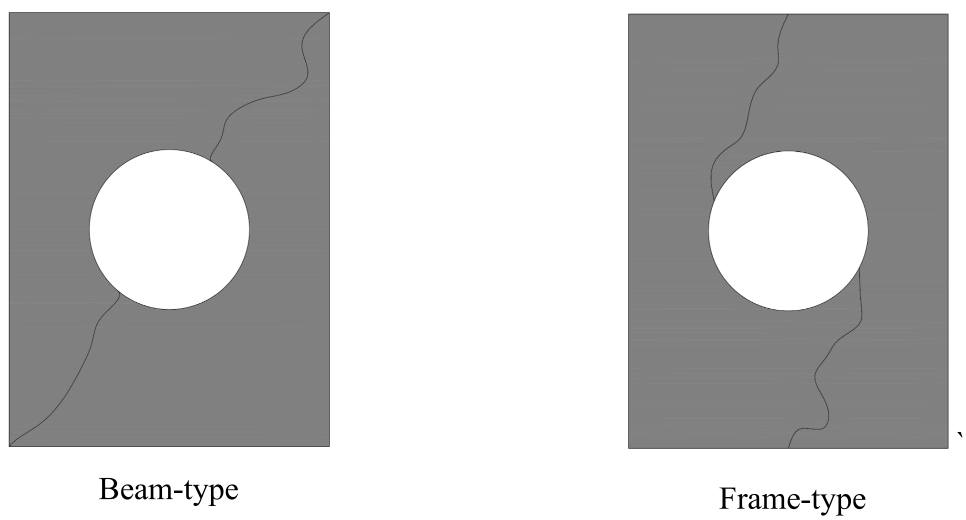

Figure 17 Shear failure modes in concrete beams at the location of the holes

Since the SEAHIVE® unit as tested falls into the category of deep members, it is appropriate to analyze it using the strut-and-tie method (STM). However, ACI 440.11 CODE [39] for the design of GFRP-RC members is silent on this approach. Hussain and Nanni (2024) have highlighted the possibilities of extending the use of STM models in ACI 318-19 [41] for GFRP-

RC members [41,42]. For this study, the provisions in CSA S806-12 [43] for STM are adopted to determine the expected capacity of the specimen.

The existing models for analyzing deep members would not be appropriate for SEAHIVE®, as it involves a complex hollow cross-section with holes. It should be noted that due to the presence of these holes, the stress flow will not be uniform, and may result in stress concentrations. For simplicity and in first approximation, the presence of holes was ignored and a model having one chord, four struts, six nodes, and two ties was assumed forming a simplified STM for SEAHIVE® (See Figure 18).

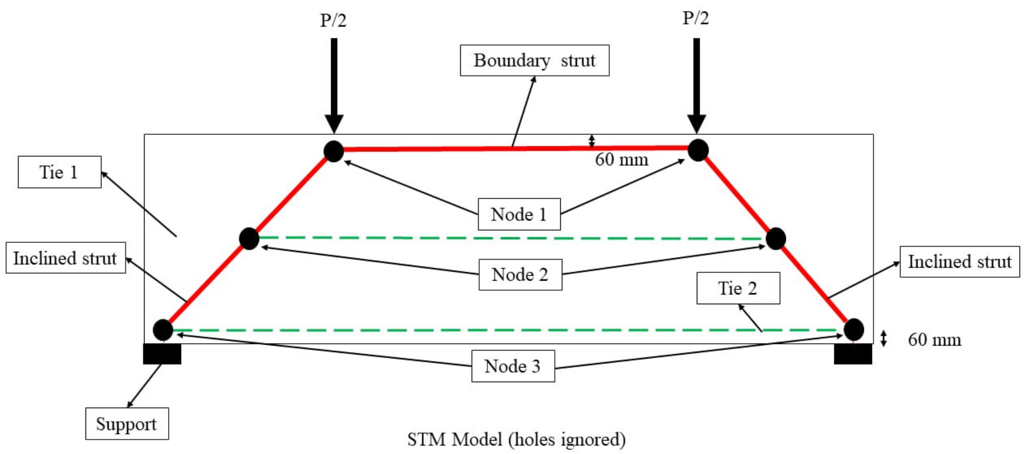

Figure 18 STM model

CSA S806-12 [43] in section 8.5.2.4 provides the relationship for determining the limiting compressive stress (f_{cu}) and strain (ε_1) in concrete struts as provided below:

θ_s = The smallest angle between the strut and the adjoining ties

ε_f = The tensile strain in the tie bar located closest to the tension face of the beam and inclined at θ_s to the strut.

The angle of inclination for the strut is conservatively assumed equal to be 40 degrees. Assuming a tension-controlled section, the strain in the tie may be taken equal to 0.0138. Thus, $\varepsilon_1$was calculated equal to -0.0291. Using the compressive strength of concrete and strain in the reinforcement, the compressive stress in the concrete strut was calculated to equal 9.64 MPa which is less than the specified limit of $0.85f'_c$ (34 MPa).

The required strength of the strut can be calculated by multiplying the stress in the strut with its cross-sectional dimensions as given below:

$$F_{nn} = f_{cu} A_s \qquad \text{Eq. 4}$$

The cross-sectional dimensions of strut can be calculated using any commercial software [42], but in the first approximation, its width was assumed equal to the concrete distance between holes (i.e., 206 mm) and thickness equal to that of the specimen wall (i.e., 127 mm). With these dimensions, the strut strength was calculated to equal 250 kN possibly representing an upper threshold. It should be noted that the presence of stirrups would provide confinement to the concrete in the strut, thereby contributing to its capacity due to tension stiffening. The effect of holes and stirrups could be explored using a numerical model based on the Finite Element Method (FEM).

The concrete strength in the nodes may be calculated as per provisions of CSA S806-12 [43], section 8.5.4.1. which impose some limits on the concrete compressive stress depending on the confinement.

It is assumed that the load is transferred from each loading knife to support a minimum of two struts with each flow of forces. One from the loading knife to the center of SEAHIVE® (assuming a node at this location bounded by struts and a tie at this location), which then transfers the loads to the node supported by another strut. Since the nodes have similar configurations (bounded by strut and anchoring one tie), only one node needs to be analyzed for determining nodal capacity. The concrete strength in the node (f_{ce}) was calculated as per CSA S806-12 [43], section 8.5.4.1(b) equal to 40 MPa. The strength of the node may be calculated by multiplying the concrete strength in the node with its dimensions as provided below:

Where A_{nz} is the area of the nodal zone. The minimum width of the bearing surface at the node was calculated to be equal to 100 mm and its thickness equal to 75 mm. Using the above dimensions, the bearing strength of the node was calculated to be equal to 300 kN.

CSA S806-12 [43] in section 8.5.3.2 states that the area of reinforcement in the tie, A_{FT}, shall be large enough to ensure that the calculated tensile force in the tie does not exceed $0.65\Phi_f A_{FT} f_{Fu}$. CSA S806-12 [43], in section 7.2.7 states that for bonded FRP reinforcement Φ_f shall be taken equal to 0.65. The area of 1-M15 bar was equal to 200 mm^2, and its ultimate guaranteed tensile strength was equal to 840 MPa. For the SEAHIVE® specimen, the maximum force limit was calculated as equal to 70 kN.

For the development of maximum tensile force in the tie, CSA S806-12 [43] states reinforcement should be capable of resisting calculated tension in the reinforcement at the location where the centroid of this reinforcement crosses the edge of the adjoining strut. For straight bars extending a distance beyond the critical location where $x < l_d$, the calculated stress shall not exceed $0.65\Phi_f A_{FF} f_{Fu}$ (x/l_d), where l_d is the required development length of the bar. l_d can be calculated as per section 9.3.2 of CSA S806-12 [43] as provided below:

$$l_d = 1.15 \frac{k_1 k_2 k_3 k_4 k_5}{d_{cs}} \frac{f_F}{\sqrt{f_c'}} A_b \qquad \text{Eq. 6}$$

d_{cs} = Smaller of:

(a) the distance from the closest concrete surface to the center of the bar being developed.

(b) two-thirds of center-to-center spacing between bars being developed, mm.

k_1 = Bar location factor taken equal to 1.3 for horizontal reinforcement placed so that more than 300 mm of fresh concrete is cast in the member below the development length or splice and 1.0 for other cases.

k_2 = Concrete density factor is taken equal to 1.3, 1.2, and 1.0 for low density, semi-low density, and normal weight concrete.

k_3 = Bar size factor is taken equal to 0.8 for $A_b \leq 300$ mm^2 and 1.0 for $A_b \geq 300$ mm^2.

k_4 = Bar fiber factor is taken equal to 1.0 for GFRP and CFRP and 1.25 for AFRP

k_5 = Bar surface profile factor is taken equal to 1.0 for surface roughened or sand-coated surfaces, 1.05 for spiral pattern surfaces, 1.0 for braided surfaces, 1.05 for ribbed surfaces, and 1.80 for indented surfaces.

In the SEAHIVE® specimens, k_1 was equal to 1.3, k_2 was equal to 1.0 for normal-density concrete, the bar size factor was equal to 0.8, the bar fiber factor was equal to 1.0, and the surface profile factor was equal to 1.0. For tension-controlled sections, f_{Fu} may be taken equal to 840 MPa. The development length was calculated to be equal to 560 mm.

CSA S806-12 [43] section 8.5.3.2 states that when the reinforcement cannot be developed for its full capacity (i.e., $x < l_d$), the calculated stresses shall be less than $0.65\Phi_f A_{FF} f_{Fu}$ (x/l_d). It may note that from the center of the node to the end of the specimen the available length is equal to 50 mm. Using the provided information the limit on maximum force in the tie was calculated equal to 19 kN.

The failure of a SEAHIVE® tested in flexure may be due crushing of concrete in the strut or node, or due to rupture of tie reinforcement, provided it is fully developed. It can be observed in Figure 13 that stress concentrations occurred at the bottom node at the support, and the specimen failed by the propagation of cracks both at the node and horizontal cracks at the center of the leg. The specimen failed at a load equal to 250 kN, which is significantly lower than the strength of the strut and nodes. It may be observed in Figure 13, that there are no signs of concrete crushing in the assumed struts and nodes except at the bottom node. However, the failure at the bottom node may be triggered by stresses in the tie reinforcement. It is worth noting that the required development length for the specimen was calculated equal to 560 mm, however, reinforcement in Tie-2 could only be developed for 50 mm.

CSA S806-12 [43] section 8.5.3.2 states that when tie reinforcement cannot be developed at the node, the maximum force in the tie shall not be greater than $0.65\Phi_f A_{FF} f_{Fu}$ (x/l_d)., equal to 19 kN. However, the force in the tie was calculated equal to 30 kN. Therefore, it may be concluded that the specimens under flexure failed as the reinforcement in the tie could not be developed for the minimum force (i.e., 19 kN).

As mentioned above due to complex geometrical configuration, no single method may define the complete failure of the specimen. Even if the specimen falls into the category of deep members, the configuration of struts is uncertain until a detailed FEM is carried out. The width of the strut was conservatively taken equal to the width of concrete between holes, but due to the presence of holes, the transfer of forces to nodes is uncertain. Therefore, for a better understanding of the failure mechanism in the SEAHIVE® specimen sophisticated FEM models should be used.

UNITS REINFORCED EXTERNALLYT WITH GFRP WRAPS

Experimental work

Test Specimens

To assess the capability of SEAHIVE®, four specimens underwent structural testing: two subjected to pure compression and two to flexure, respectively. The configuration and preparation details of each specimen are outlined in Table 4 and illustrated in Figure 19.

Table 4 Configuration of SEAHIVE® samples

Specimen ID	D/t*	Loading type	Specimen Length (mm)	Characteristics	Objectives
CS-1	0.25	Monotonic quasi-static	910	Hollow unit with bonded GFRP	Study the
CS-2	0.25	pure compression	910	(203- mm dia.)	effect of pure compression
FS-1	0.25	Monotonic quasi-static	1830	circular reinforced with externally-	and bending on the structural
FS-2	0.25	flexure	1830	perforations	performance

notes D/t *= side perforation diameter to total height of the unit

The total span length used for the flexural test was 1.83 meters, as depicted in Figure 19(a), a dimension aligned with production specifications. As for the compression test, specimens were cut in to two parts by saw-cutting, resulting in two elements, each with a length of 0.91 m. The diameter of the holes on the hexagon was 203 mm, spaced at a center-to-center distance of 346 mm, as illustrated in Figure 19(a). Each leg of the GFRP-RC hexagon measured 440 mm in length and 127 mm in thickness. The overall depth of the cross-section was 792 mm as depicted in Figure 19(b). The SEAHIVE® elements were transversally pretensioned with resin-impregnated fiberglass, as illustrated in Figure 19(c). The width of prestressing wraps and the distance between them equals 50 mm and 40 mm, respectively (See Figure 19(a)).

For the SEAHIVE®, GFRP strips made of resin-impregnated fiberglass roving were applied to each edge using the wet layup method, with 10 roving applied to each edge (about 10 mm^2 cross section area of GFRP pack). Subsequently, GFRP wraps made of resin-impregnated fiberglass roving were applied around the hexagonal section, with 250 N of tension applied to each roving during the wrapping process. Each wrap was positioned as close as possible to the holes, to compensate for the lower shear capacity at these locations. In addition to compressing the concrete, these wraps have the function of anchoring the longitudinal strips by enhancing the bond between strip and concrete. This is because the pretensioned wrap creates a compressive force at each corner between strips and concrete thus significantly increasing the shear force capacity between them (See Figure 19(d)). For each wrap, 80 turns of 2400 Tex E-glass roving were applied (about 80 mm^2 cross section area of GFRP pack), with each wrap tensioned to a total of 20 kN. The 250 N tension applied to each 2400 Tex roving is approximately 25% of its ultimate tensile capacity (refer to Table 5) which is below the limit of creep-rupture for GFRP [44].

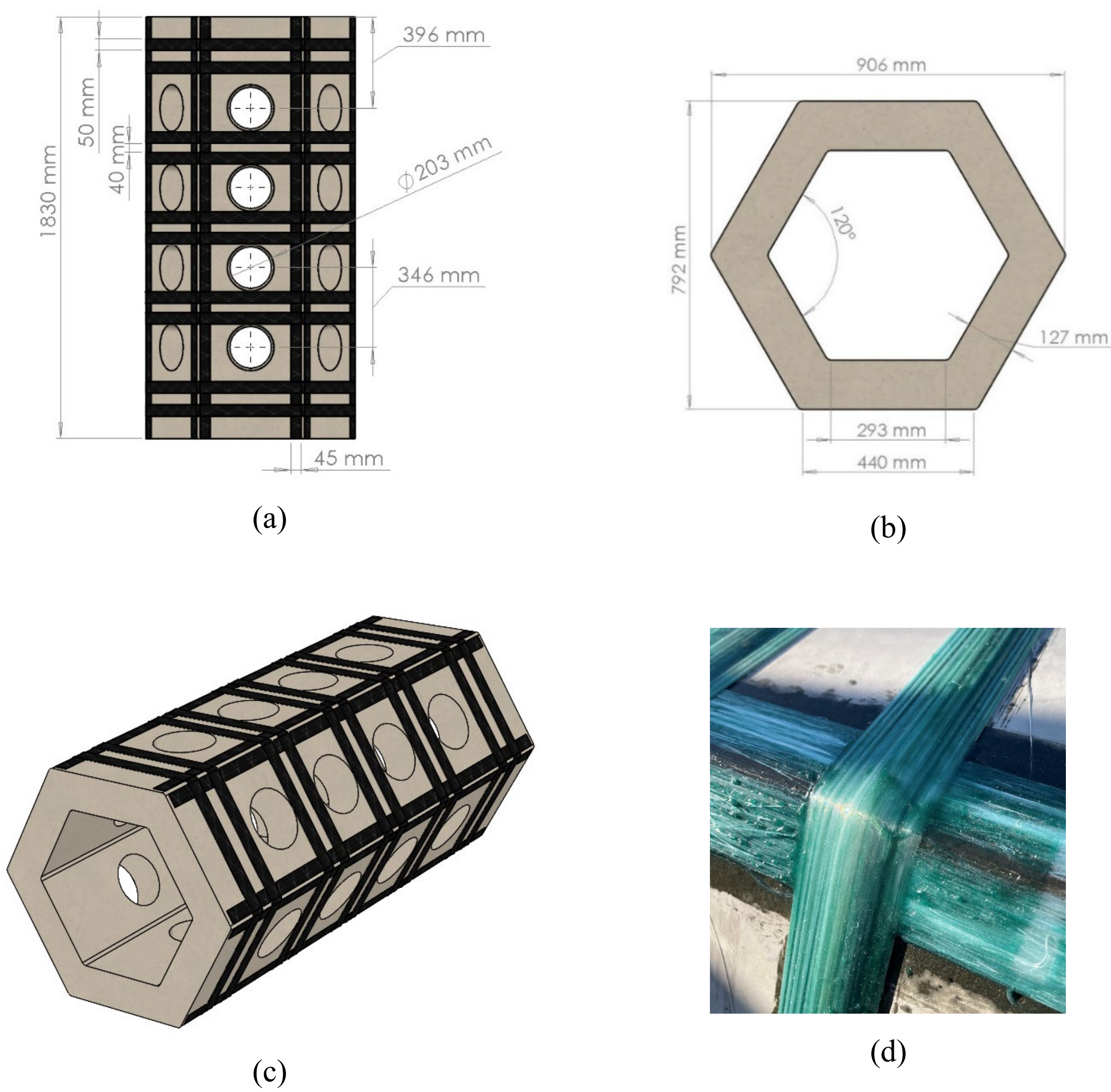

Figure 19 Geometry of the SEAHIVE® unit with reinforcement details

Materials

GFRP Characterization

The fiberglass used for wrapping is 2400 Tex E-glass, was paired with a high-modulus epoxy Elan-tech® EC 152/W 152 MR. The specifications from the manufacturer are based on ASTM D1475-13 [45] for resin and ASTM D2343-17 [46] for fiberglass. The minimum guaranteed tensile capacity is 0.4 N/Tex, with a typical strength of 1151 N for a 2400 Tex epoxy-impregnated roving. The typical Young's modulus for the impregnated roving is 81.2 GPa, based on tests conducted on a single roving.

For more accurate data on the mechanical performance of the GFRP strips and wraps, experimental testing was conducted. The tensile properties of the GFRP samples were determined following the provisions of ASTM D2343 [46]. Three cylindrical samples were wrapped with 40 turns of fiberglass roving (see Figure 20(a)), each. subjected to a pretension of 200 N. During the test, the cylinders, separated in halves, were tensioned till GFRP failure. After three tests, the average ultimate tensile strength was approximately 100 kN. The standard deviation of the samples from these tests was found to be 29.3 kN. Given that there were 40 turns, this equates to approximately 1250 N per roving (refer to Figure 20(b)).

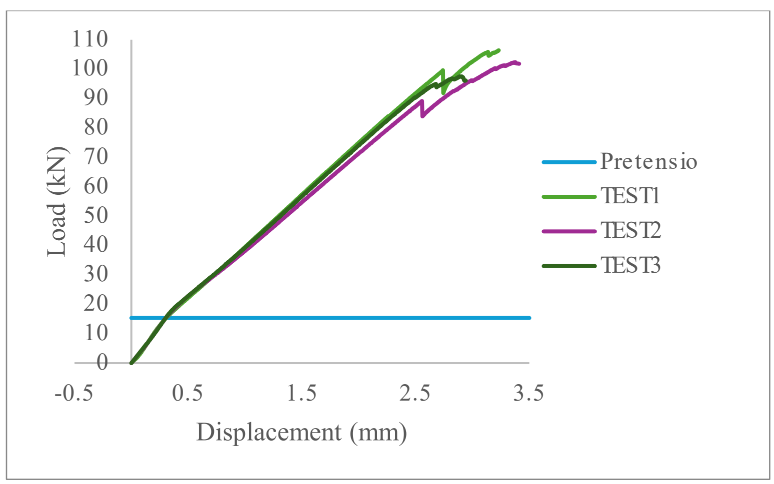

(a) (b)

Figure 20 GFRP tensile test: (a) samples and (b) load-displacement results (courtesy of CIRI Edilizia e Costruzioni, DICAM, University of Bologna, Italy; Drs. Anna Rosa Tilocca and Andrea Incerti; Prof. Marco Savoia, Director)

Concrete Characterization

The concrete used to build the SEAHIVE® units adheres to the C30/37 type, ensuring it meets specific strength and durability criteria. According to EN 1992-1-1 [47], for the purposes of both analysis and testing, the characteristic compressive strength (f_{ck}) of concrete is assumed to be 30 MPa and 2.9 MPa as tensile strength (f_{ct}).

Table 5 Material properties of fiberglass and concrete

Designation	Specification	Density (g/cm³)	Elastic modulus (MPa)	Ultimate tensile strength (f_{fu}) (MPa)	Ultimate Tension Force (N)	Ultimate strain	Concrete strength (MPa)
Fiberglass	2400 Tex	2.54	81,200	1280	1250	0.034	N/A
Concrete	C30/37	2.5	32,837	N/A	N/A	0.003	30.0

Test Set-up and Instrumentation

Hal Unit under Pure Compression

The experimental configuration for the compressive test is illustrated in Figure 21(a) and (b), for specimens measuring 910 mm in length. To ensure an even distribution of the applied load from the hydraulic jack across the surface of the element, two masonite sheets measuring 914 x 457 x 5 mm were placed on the element's surfaces. Following this, two steel plates measuring 900 x 400 x 25 mm were positioned one on top and one on bottom of the specimens. Subsequently, load cells were situated over the sample, and the load was applied using a hydraulic jack.

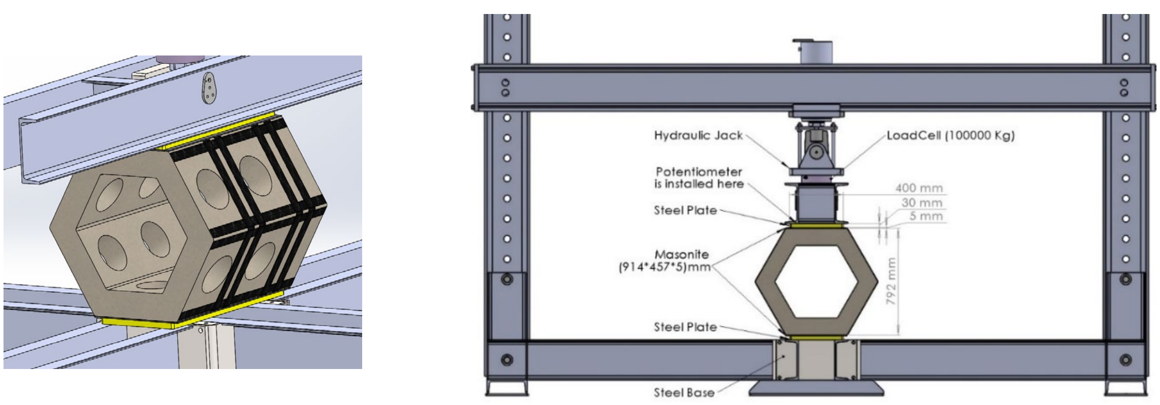

(a) (b)

Figure 21 Sketch of compression test configuration: (a) profile and (b) cross-sectional view

Unit under Flexure

Two full-size units were tested under four-point bending to investigate the flexural behavior of the specimens. As shown in Figure 22(a), (b) and (c), the distance between a support and a loading point (i.e., shear arm=a) is 627 mm, while the total height of the sample (i.e., h) is approximately 792 mm. The a/h ratio is about 0.8 (See Figure 22(c)), indicating that the unit being tested can be characterized as a deep beam. Two steel plates (25x25x700 mm) were used as the loading knives positioned over the center of the middle holes.

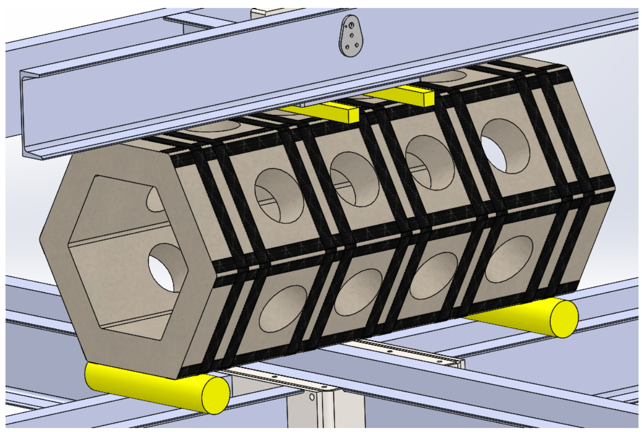

(a)

(b)

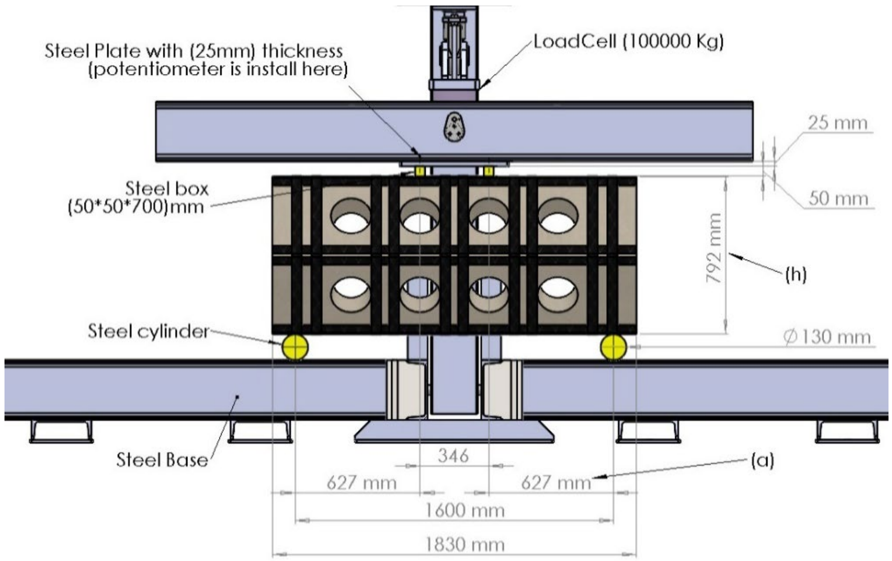

(c)

Figure 22 Flexural test configuration: (a) 3D schematic view, (b) specimen photograph; and (b) schematic view of the loading frame with dimensions

Loading Protocol

Four specimens underwent testing: two were subjected to pure compression, and two to flexural testing. Quasi-static load protocols were applied for both compression and flexural tests, with each specimen loaded monotonically until failure occurred.

Results and Discussion

This section provides information on experimental results regarding crack patterns and load-displacement curves for both pure compression and bending tests. The first cracking load, ultimate loads, and maximum displacement or mid-span deflection were recorded.

Compression Test Results

Crack Pattern and Failure Mode:

In Figure 23(a), the CS-1 specimen is shown at the point of failure. Cracks are evident along the mid-length of the horizontal section and at the corners of the inclined legs. Initially, horizontal cracks developed, followed by inclined cracks likely attributed to shear. The failure occurred as the horizontal cracks extended, ultimately connecting with the holes in the hexagon. Similarly, the crack pattern observed in the CS-2 specimen (depicted in Figure 23(b)) closely resembled that of the CS-1 specimen.

The presence of external reinforcement effectively prevented the sudden failure of the samples after the first cracks were initiated. It seems the compressive pressure induced by the external reinforcement significantly increased the strength of the specimens under pure compressive load. The pretensioned wraps created a compressive force along the edges of the SEAHIVE®'s hexagonal structure. This mitigated the effect of tensile stresses on the specimen. As a result, the ultimate strength of the SEAHIVE® became dependent on the GFRP ultimate strength.

During the test, the SEAHIVE® successfully resisted the applied force until some of the glass filaments reached their limit and broke with concrete cracks that began to propagate. The first cracks appeared at the outer points of the SEAHIVE®, where the applied load generated maximum moments. Finally, two additional cracks appeared in the middle of the SEAHIVE® top and bottom legs due to the deformation of the specimen around the center.

(a) (b)

Figure 23 Cracking pattern at failure in (a) CS-1 (b) and CS-2

Load Displacement Curves:

Figure 24 shows the load-displacement diagram of CS-1 and CS-2 tested under pure compression. The horizontal axis indicates the average displacement, and the vertical axis shows the applied load. The first crack occurrence is shown in the diagram by a load drop in both CS-1 and CS-2 around 145 and 172 kN, respectively. After that, the specimens continued to carry the load until GFRP failure (about 358 kN for both).

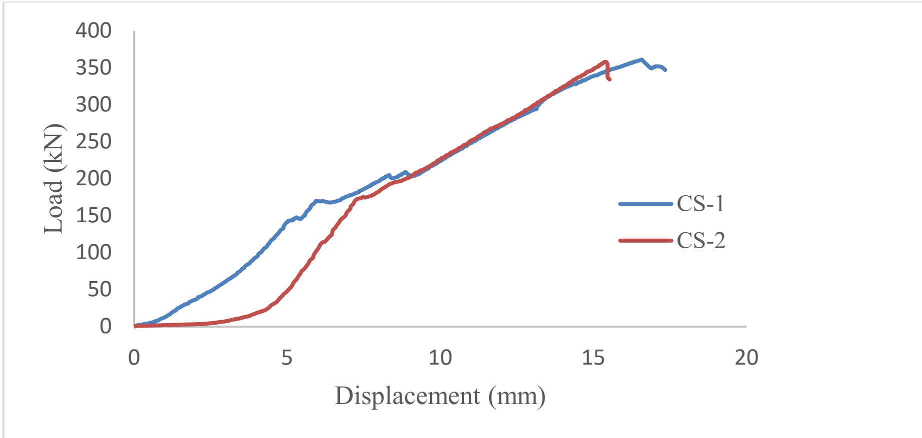

Figure 24 Load-displacement results of pure compressive tests

Flexure Test Results

Crack Pattern and Failure Mode:

Figure 25(a) and (b) show the failed specimens tested under bending. The cracks started to propagate in the middle of the SEAHIVE® at the holes and extended directly upwards. This crack pattern suggests failure due to bending moment in the area where the moment of inertia is minimal due to the presence of holes. When the longitudinal GFRP strips placed on the bottom (first) and mid-height (second) corners could no longer withstand the tensile stress, they failed and caused the collapse of the specimen.

(a) (b)

Figure 25 Cracking pattern at failure of (a) FS-1 and (b) FS-2

Load Displacement Curves:

Figure 26 shows the load-displacement diagram for FS-1 and FS-2, where the horizontal axis represents the average displacement, and the vertical axis indicates the applied load. According to the experimental data, the first drop in load for specimens FS-1 and FS-2 occurred at approximately 81 and 86 kN, respectively. Additionally, the final loads for FS-1 and FS-2 were 227 and 315 kN, respectively.

The difference between the two results is due to the slipping of the longitudinal strips. In the FS-1 test, the GFRP strips held together until 231 kN, but then suddenly slipped due to inadequate anchorage provided by the transverse wraps. Moreover, in this test, the longitudinal strips were adhered using the layup method without any anchors at both ends.

In the FS-2 specimen, to overcome slippage, the longitudinal strips were anchored at both ends of the SEAHIVE®. A slot was created at each end, and during the placement of the longitudinal fibers using the layup method, each fiber filament was wrapped around the slot. As a result, the pack of fibers became securely anchored at each end (See Figure 27). During the test of FS-2 specimen, at 3.9 mm displacement, some of the longitudinal strip partially broke, resulting in a loss of load capacity. However, the remaining strip portions continued to hold, allowing the specimen to sustain a higher load. After a peak load was reached, fibers started to break gradually until sudden failure. Overall, the SEAHIVE® in FS-2 withstood up to 315 kN before complete failure, which is significantly higher than the load in the FS-1 test. Table 6 summarizes the results of the experiments on four tested specimens.

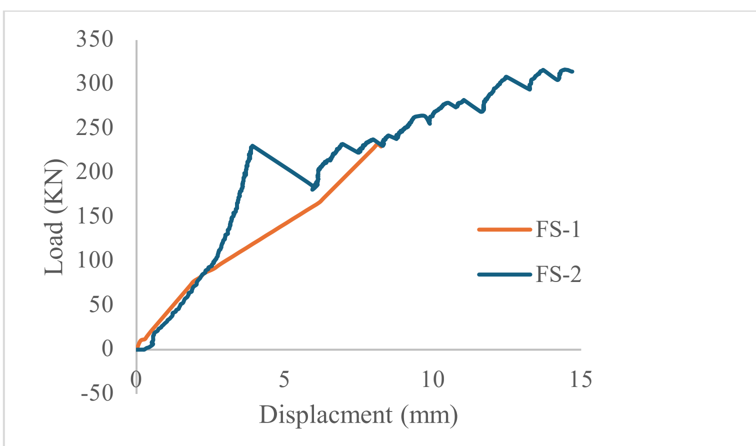

Figure 26 Load-displacement results of FS-1 and FS-2

Figure 27 Anchoring fibers on both ends of the longitudinal strips for FS-2

Table 6 Results of the experimental test on specimens

Load or Deflection	CS-1	CS-2	FS-1	FS-2
First cracking load (kN)	145	172	73	75
Ultimate load (kN)	360	354	227	315
Maximum deflection (mm)	17	15	8.3	14.68

Analysis

Specimens under Compression

It was observed in Figure 28 that the first cracks appeared at of the end of the inclined leg. The failure at this location resulted from the combined effect of axial and flexural stresses resulting from applying pure compression and prestressing load resulting from the GFRP wraps (See Figure 28).

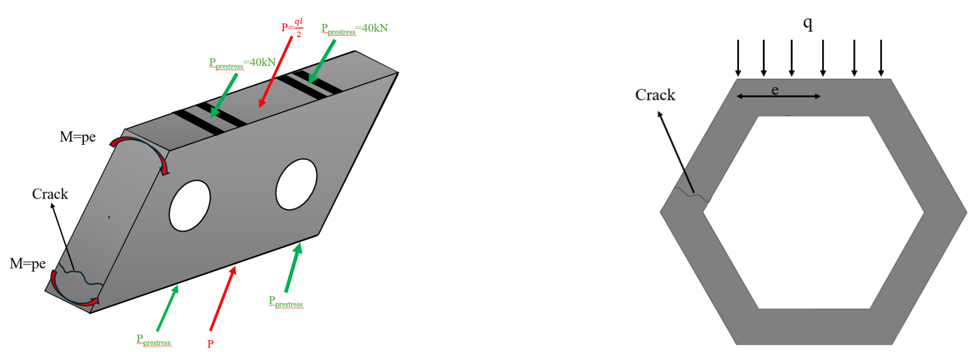

Figure 28 Loads on inclined leg

The effective moment of inertia of the leg cross-section was calculated by subtracting the moment of inertia of two holes from the gross cross-section moment of inertia of the solid leg resulting in $I = 155335710\ mm^4$. The corresponding cross-sectional area equals $A = 115570\ mm^2$. The first visible cracks on the specimen appeared at a load between 145 and 172 kN, as per Table 6. Therefore, the load on each leg was assumed to be equal to about 72.5 kN. The moment at the mid-end of the leg was calculated by multiplying the applied load with its eccentricity (e) assumed to be e=144 mm (See Figure 28). The stress at cracking was calculated as $\sigma_b = -4.2$ MPa.

The tensile modulus of rupture in concrete inclusive of the effect of prestressing was calculated to be equal to 4.08 MPa, showing that capacity is lower than applied stress (i.e., 4.2 and 4.08 MPa); thus, causing the first crack that eventually led the failure. Even though not strictly applicable to this case, ACI 440.11-22 [39] provisions were used to calculate the moment capacity of the section (M_n) compared to the cracking moment (M_{cr}). Moment capacity equals 10022 kN.mm and cracking moment equals 100489 kN.mm indicating that a brittle failure would be expected.

To evaluate the performance of the element under pure compression, a Finite Element Method (FEM) analysis was also performed using the full SEAHIVE®. As shown in Figure 29, the SEAHIVE® under pure compressive load experienced the maximum stress on the outer edge of the inclined legs of the hexagon. These areas correspond with the locations where cracks initiated in the actual specimens during testing.

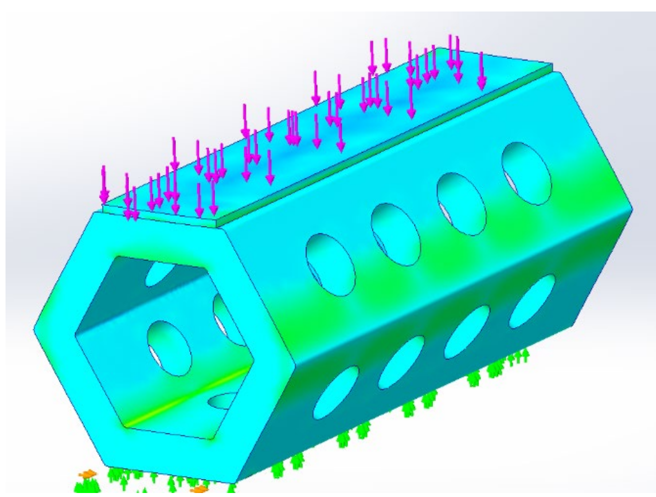

Figure 29 Stress distribution on the SEAHIVE® under compression load

Specimens under Flexure

Gohari's findings [40] indicated that when the diameter of holes on the surface of concrete beams subjected to bending exceeds 0.25 times the total depth of the beam, traditional beam theory becomes inapplicable. In this study, with a hole diameter of 203 mm and eight holes on each side of the unit (four holes stacked vertically), the ratio of hole diameter to the total depth of the concrete surpasses 0.25, as per the limit set in the referenced study. The presence of holes on all surfaces of the hexagonal, hollow specimen complicates the analysis. Moreover, the shear span-to-reinforcement depth ratio of the SEAHIVE® was equal to 0.8, indicating that conventional beam theory is unsuitable for analysis.

To evaluate the performance of the element under flexural load, a FEM analysis was performed using the full SEAHIVE®. As shown in Figure 30(a) and (b), the SEAHIVE® was modeled under a flexural load while seated on two cylindrical fixtures at both ends, simulating the test conditions. The FEM model displayed maximum tensile stress at the bottom surface of the unit at the location where the bending moments is greatest. Additionally, near the holes, in the direction pointing to the loading knives, maximum stress was observed. These red areas in Figure 30(a) and (b) correspond with the locations where cracks initiated in the actual specimens during testing, illustrating the pattern of crack growth direction in the specimen.

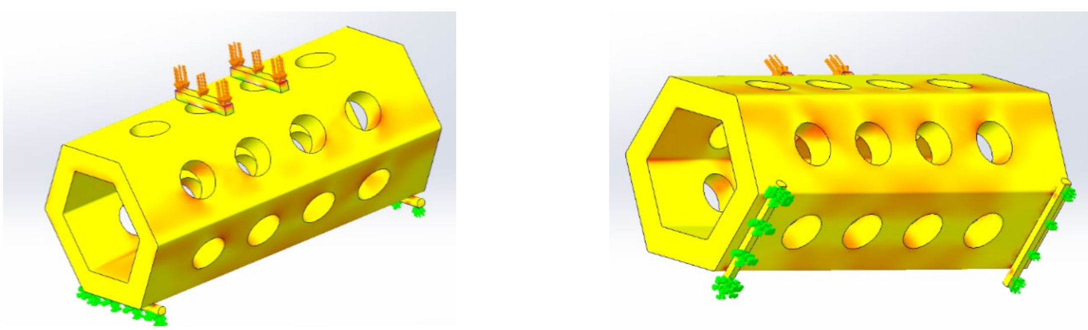

(a) (b)

Figure 30 Stress distribution on the SEAHIVE® under flexure (a) 3D view, (b) bottom of specimen view

DIMENTIONAL ANALYSIS TO COMPARE TEST RESULTS

Based on Harris et al. [48] "Any Models need to be crafted, loaded, and interpreted based on a set of principles that connect the model to the original structure. These principles are grounded in modeling theory, which stems from a dimensional analysis of the physical phenomena influencing the structure's behavior [48]. To summarize its definition, dimensional analysis is an analytical tool to develop a similitude between the model and prototype".

Dimensions and Homogeneity

The use of dimensional analysis has a long history, originating when humans first tried to define and measure physical quantities. These descriptions needed two main characteristics: qualitative and quantitative.

The qualitative characteristic enables the description of physical phenomena through essential natural measurements. Mechanical (both static and dynamic), thermodynamic, and electrical issues are qualitatively defined using these basic measurements:

- Length (L)

- Force (or mass) (F)

- Time (T)

- Temperature

- Electric charge

The quantitative characteristic involves both a number and a standard of comparison. For example, velocity has dimensions of LT^{-1}, and units such as mph, ft/sec, and knots. In structural modeling, which often involves mechanical problems, the measures of length, force, and time are the most crucial [48]. The theory of dimensions can be categorized into two key principles as follows:

Dimensional Homogeneity of Equations

Any mathematical description (i.e., equation) that represents a natural phenomenon must be dimensionally homogeneous. This means the equation must remain valid regardless of the dimensional units used to measure the physical variables. For example, the equation for bending stress, $\sigma = \frac{MC}{I}$, holds true whether force and length are measured in Newtons and meters, pounds and inches, or any other consistent units [48].

Dimensionless Form of Equations

Given that all governing equations must be dimensionally homogeneous, any equation of the form

$$F(X_1, X_2, \dots, X_n) = 0 \qquad \text{Eq.7}$$

can be rewritten in the form

$$G(\pi_1, \pi_2, \dots, \pi_m) = 0 \qquad \text{Eq.8}$$

where the π terms are dimensionless products of the n physical variables $X_1, X_2, \dots, X_n$, and $m = n - r$, with r being the number of fundamental dimensions involved. This second principle has two significant implications. First, Deducing Physical Phenomena that is the form of a physical phenomenon can be partially inferred by carefully considering the dimensions of the involved physical quantities X_i. Second, Similitude in Modeling is physical systems that differ only in the magnitudes of the units used to measure the quantities X_i, such as a prototype structure and its scaled-down model, will have identical functional forms G. Achieving similitude in modeling involves ensuring that the dimensionless π terms are equal in both the model and the prototype, which is essential for the complete functional relationships to be identical.

Dimensional Analysis of Tested Elements

In this research, the modulus of rupture is considered to relate the strength of the element reinforced with GFRP wraps to the element reinforced internally with GFRP bars. As can be seen in sections 2 and 3, the two elements resemble in terms of geometric parameters. The differences between these two elements can be categorized into two aspects, namely, concrete compressive strength and reinforcement amount. It should be noted that the effect of prestressing is considered in the calculation of the modulus of rupture (f_r), and the effect of geometry is considered in the moment of inertia (I). Figure 31 shows the intended leg in elements reinforced with GFRP wraps for the calculations.

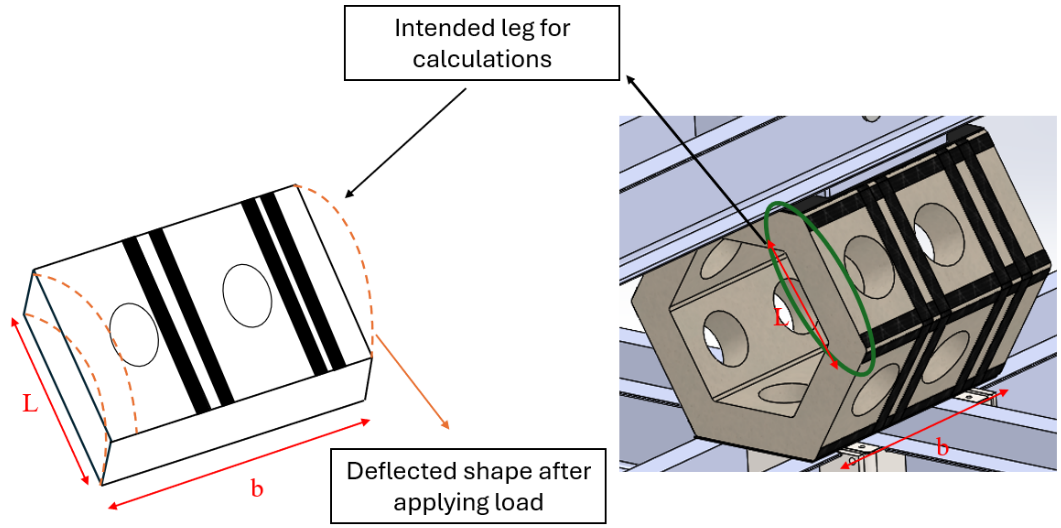

Figure 31 Intended leg for calculations in elements reinforced externally with GFRP wraps

$$F(f_r, C, I, M) = 0 \qquad \text{Eq. 9}$$

Where f_r is the modulus of rupture for elements. It should be noted that the effect of prestressing is considered in the calculation of f_r as can be seen in section 3. C_t is the depth neutral axis, I is the moment of inertia of the element in the location of the crack (See Figure 32), and M is the cracking moment.

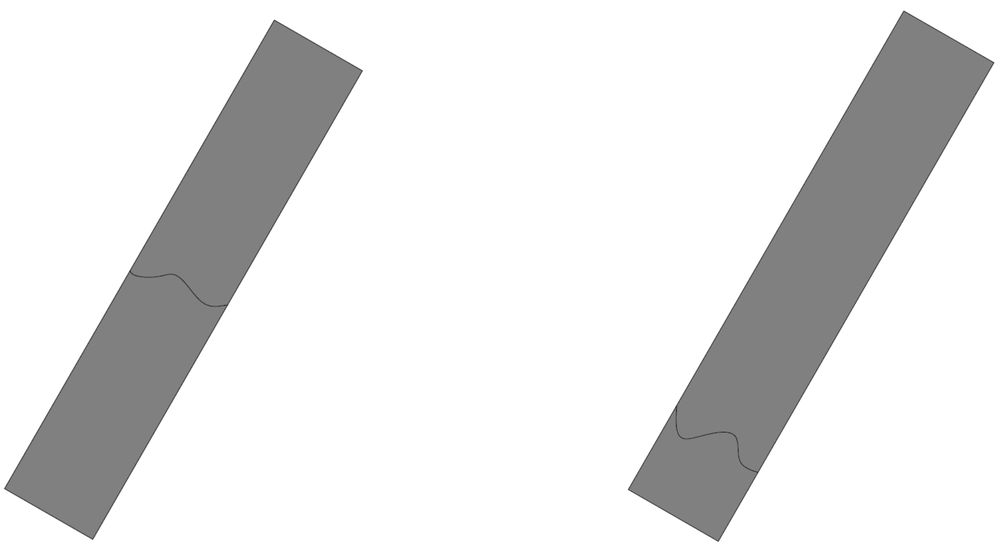

(a) (b)

Figure 32 Location of the cracks in (a) elements reinforced with GFRP bars and (b) elements reinforced with GFRP wraps

$$\frac{M_{ext\ reinf}}{M_{int\ reinf}} = \frac{f_{r_{ext\ reinf}}}{f_{r_{int\ reinf}}} \times \frac{I_{ext\ reinf}}{I_{int\ reinf}} \times \frac{C_{t\ int}}{C_{t\ ext}} \qquad \text{Eq.10}$$

With regards to the sections 2 and 3, $f_{r_{ext\ reinf}}$ and $f_{r_{int\ reinf}}$ equal to 4.08 and 3.92 MPa and $I_{ext\ reinf}$ and $I_{ext\ reinf}$ equal to 155335710 and 86885578 mm^4, respectively (Please refer to section 2.6.1 and section 3.6.1 for the calculation of f_r and I). Moreover, C_t is calculated. These values are presented in Table 6.

Table 7 parameters

Unit	f_r (MPa)	I (mm^4)	C_t (mm)
CB-1 CB-2	3.92	86,885,578	55.5
CS-1 CS-2	4.08	155,335,710	117.2

After doing some calculations, the relation factor of the two elements to relate final strength is about 1.13. It shows that for relating the experimental results of the final strength of the elements reinforced internally with GFRP bars must be multiplied by 1.13 to be comparable with the experimental results of the element externally reinforced with GFRP wraps. Hence, in this case, elements reinforced externally are a prototype and the relation factor will be applied to the results of the element internally reinforced with GFRP bars.

In order to relate the displacement λ of the two elements, Elastic modulus E, moment of inertia I, length L and applied load P are considered a key parameter.

$$F(E, l, I, P, \lambda) = 0 \qquad \text{Eq.11}$$

In this research, as the length of the two elements (L) and thickness of the element are the same I is not considered in calculations. Moreover, as the elastic modulus is related to the compressive strength of the concrete, ACI 318 [49] is used for the calculation of elastic modulus. After doing some calculations, the relation factor of the two elements is about 1.16. It shows that for relating the displacement results of the elements reinforced internally with GFRP bars must be multiplied by 1.16 to be comparable with the experimental results of the element externally reinforced with GFRP wraps. Figure 33 shows the experimental results after applying the relation factor.

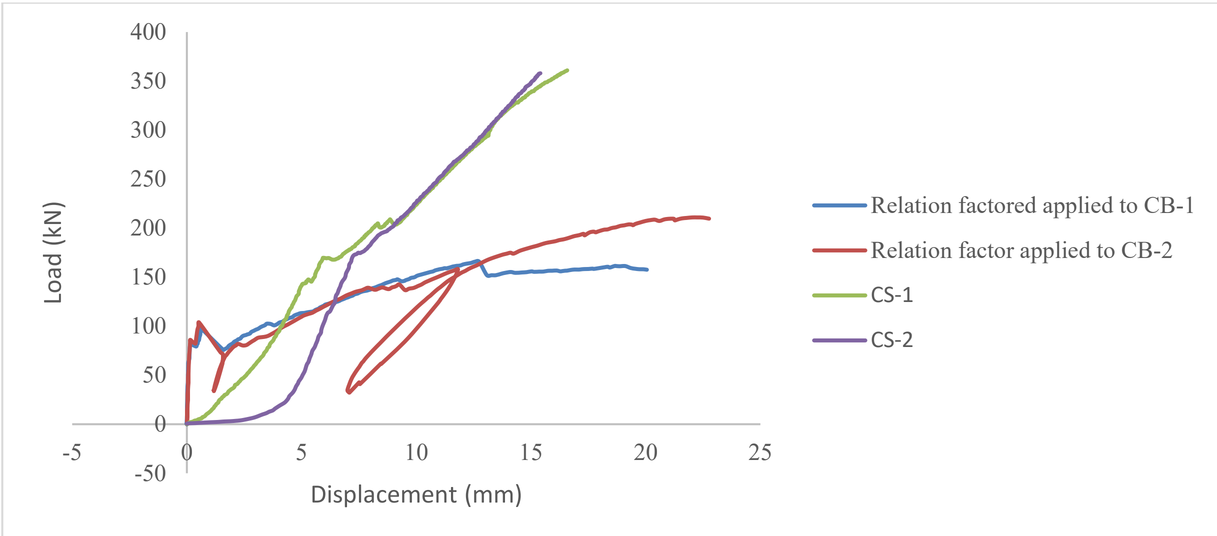

Figure 33 Compression results of experiments after applying relation factors

RECOMMENDATIONS AND CONCLUSIONS

The study was conducted to analyze the structural performance of SEAHIVE® reinforced with either internally GFRP bars or externally bonded GFRP longitudinal strips and pretensioned transverse GFRP wraps. The latter reinforcement methodology applied to dry-cast concrete appears to be effective. The study examined the structural behavior of hexagonal, hollow, and perforated units under both pure compression and flexure. Based on the outcomes of this study the following conclusions are drawn:

Internal Reinforcement

1- The presence of internal GFRP longitudinal and transverse reinforcement in the amounts provided did not help increase the specimen's capacity due to the configuration of SEAHIVE®. In this instance, the main function of the provided reinforcements was to prevent disintegration after the failure occurred.

2- In the bending test, span-to-height ratio was equal to 0.8 and this, in addition to the presence of holes and the hollow hexagonal shape, prevents analysis with classical beam theory. Sophisticated STM models may appropriately assess capacity with ACI 440.11-22 and CSA S806-12, but numerical modeling may be the only answer.

3- The specimens tested under pure compression failed when the stresses exceeded the tensile capacity of the concrete on the inclined legs of SEAHIVE®. There was no reinforcement to resist crack propagation after the onset of concrete cracking in the case of internal reinforcement.

4- The internally reinforced specimens tested under flexure failed as the longitudinal reinforcement in tension was not properly anchored and the concrete toe crushed.

External reinforcement

5- The method of dry-casting coupled with external reinforcing presents several potential benefits, including the use of relatively inexpensive raw materials, easy automation, high productivity, and reduced need for reinforcing material due to the tensioned application of GFRP wraps on the product surface.

6- The experimental results closely matched the predictions from the Finite Element Method (FEM) analysis, validating the accuracy and reliability of the FEM as a design tool for optimizing the reinforcing process in terms of amount as well as pre-tensioning.

7- The pretension wrapping method enhances the bond between the longitudinal GFRP strips and the concrete delaying the onset of catastrophic failure.

DATA AVAILABILITY STATEMENT

All raw data that support the findings of this study are in the Zenodo Data Share repository with the identifier https://doi.org/10.5281/zenodo.13519673.

REFERENCES

[1] National Oceanic and Atmospheric Administration, Ocean and Coastal Resource Management in Your State: States and Territories Working With NOAA on Ocean and Coastal Management, 2011.

[2] G.A. Maul, I.W. Duedall, Demography of coastal populations, Encyclopedia of Coastal Science (2019) 692–700.

[3] M. Ghiasian, J. Carrick, C. Bisson, B.K. Haus, A.C. Baker, D. Lirman, L. Rhode-Barbarigos, Laboratory quantification of the relative contribution of staghorn coral skeletons to the total wave-energy dissipation provided by an artificial coral reef, J Mar Sci Eng 9 (2021). https://doi.org/10.3390/jmse9091007.

[4] J.R. Houston, The economic value of beaches, Citeseer, 2002.

[5] A.B. Smith, US Billion-dollar weather and climate disasters, 1980-present, (2022).

[6] S. Ghiasian, R. Mohammad, Structural Morphogenesis of Green/Gray Coastal Infrastructure: Paradigms for Shoreline Protection, n.d. https://scholarship.miami.edu/esploro/outputs/991031689717602976/filesAndLinks?institution=01UOML_INST&index=null.

[7] R.S. Thomas, B. Hall, Seawall design, Butterworth-Heinemann, 2015.

[8] N. Hosseinzadeh, M. Ghiasian, E. Andiroglu, J. Lamere, L. Rhode-Barbarigos, J. Sobczak, K.S. Sealey, P. Suraneni, Concrete Seawalls: Load Considerations, Ecological Performance, Durability, and Recent Innovations, (2021).

[9] R.K. Gittman, S.B. Scyphers, C.S. Smith, I.P. Neylan, J.H. Grabowski, Ecological consequences of shoreline hardening: a meta-analysis, Bioscience 66 (2016) 763–773.

[10] A. Harasti, G. Gilja, K. Potočki, M. Lacko, Scour at bridge piers protected by the riprap sloping structure: A review, Water (Switzerland) 13 (2021). https://doi.org/10.3390/w13243606.

[11] R. Farooq, A.R. Ghumman, Impact assessment of pier shape and modifications on scouring around bridge pier, Water (Switzerland) 11 (2019). https://doi.org/10.3390/w11091761.

[12] K. Wardhana, F.C. Hadipriono, Analysis of recent bridge failures in the United States, Journal of Performance of Constructed Facilities 17 (2003) 144–150.

[13] R.K. Gittman, S.B. Scyphers, C.S. Smith, I.P. Neylan, J.H. Grabowski, Ecological consequences of shoreline hardening: a meta-analysis, Bioscience 66 (2016) 763–773.

[14] P.F. Lagasse, Countermeasures to protect bridge piers from scour, Transportation Research Board, 2007.

[15] B.W. Melville, S.E. Coleman, Bridge scour, Water Resources Publication, 2000.

[16] J. Unger, W.H. Hager, Down-flow and horseshoe vortex characteristics of sediment embedded bridge piers, Exp Fluids 42 (2007) 1–19.

[17] H.N.C. Breusers, A.J. Raudkivi, Scouring: hydraulic structures design manual series, vol. 2, Crc Press, 2020.

[18] J.C. Fischenich, M.N. Landers, Computing scour, (2000).

[19] C. Wang, X. Yu, F. Liang, A review of bridge scour: mechanism, estimation, monitoring and countermeasures, Natural Hazards 87 (2017) 1881–1906. https://doi.org/10.1007/s11069-017-2842-2.

[20] M.A.M.M.A. Mansur, K.-H. Tan, W.W.W. Weng, Analysis of concrete beams with circular web openings using strut-and-tie models, Malaysian Journal of Civil Engineering 18 (2006).

[21] M.A. Mansur, K.-H. Tan, Concrete beams with openings: analysis and design, CRC Press, 1999.

[22] S. Amiri, R. Masoudnia, M.A. Ameri, A review of design specifications of opening in the web for simply supported RC beams, Journal of Civil Engineering and Construction Technology 2 (2011) 82–89.

[23] K.-H. Tan, M.A. Mansur, Design procedure for reinforced concrete beams with large web openings, Structural Journal 93 (1996) 404–411.

[24] J.J. Daniel, J. Revathy, Experimental investigation on flexural strength of beams with opening, Int J Res Manage Tech (IJRMT) 4 (2014) 141–143.

[25] S.A. Al-Sheikh, Flexural behavior of RC beams with opening, Concrete Research Letters 5 (2014) 812–824.

[26] S. Aykac, M. Yilmaz, Behaviour and strength of RC beams with regular triangular or circular web openings, Journal of the Faculty of Engineering and Architecture of Gazi University 26 (2011).

[27] B. Aykac, I. Kalkan, S. Aykac, Y.E. Egriboz, Flexural behavior of RC beams with regular square or circular web openings, Eng Struct 56 (2013) 2165–2174.

[28] C. Yang, L. Li, J. Li, Service life of reinforced concrete seawalls suffering from chloride attack: Theoretical modelling and analysis, Constr Build Mater 263 (2020) 120172.

[29] C.C. Steputat, S. Nolan, L. Denty, P.A. Kaminski, A. Nanni, A seawall constructed with GFRP bars as structural reinforcing, Concrete International 41 (2019) 26–30.

[30] M. Balah, S. Abdel-Mawla, Efficiency of permeable caisson seawall reinforced with fibre reinforced polymers, in: Composite Materials in Concrete Construction: Proceedings of the International Seminar Held at the University of Dundee, Scotland, UK on 5–6 September 2002, Thomas Telford Publishing, 2002: pp. 265–275.

[31] A. Nanni, T.E. Boothby, C.E. Bakis, Test Methods for FRP-Concrete Systems Subjected to Mechanical Loads: State of the Art Review, Journal of Reinforced Plastics and Composites 14 (1995) 524–558. https://doi.org/10.1177/073168449501400601.

[32] A. Nanni, A. De Luca, H. Jawaheri Zadeh, Reinforced Concrete with FRP Bars, 2014. https://doi.org/10.1201/b16669.

[33] A. Al-Rahmani, F.H. Abed, Numerical investigation of hybrid FRP reinforced beams, 2013 5th International Conference on Modeling, Simulation and Applied Optimization, ICMSAO 2013 (2013). https://doi.org/10.1109/ICMSAO.2013.6552565.

[34] V.L. Brown, C.L. Bartholomew, FRP reinforcing bars in reinforced concrete members, ACI Mater J 90 (1993) 34–39. https://doi.org/10.14359/4034.

[35] M.H.Z.K.N.N.A. Mirdarsoltany, Strength Performance of Hexagonal, Hollow, and Perforated Concrete Units, Structures (n.d.).

[36] Standard Test Method for Tensile Properties of Fiber Reinforced Polymer Matrix Composite Bars, (n.d.). https://doi.org/10.1520/D7205_D7205M-06.

[37] Standard Test Method for Compressive Strength of Cylindrical Concrete Specimens, (n.d.). https://doi.org/10.1520/C0039_C0039M-21.

[38] A. Ergün, G. Kürklü, Assessing the Relationship between the Compressive Strength of Concrete Cores and Molded Specimens, 2012.

[39] A. 440.1R-15, Guide for the Design and Construction of Structural Concrete Reinforced with Fibre-Reinforced Polymer (FRP) Bars, Aci 440.1R-15 (2015) 88. www.concrete.org.

[40] S. Gohar, H.M. Afefy, N.M. Kassem, S.E.D.F. Taher, Flexural performance of self-compacted perforated concrete beams under repeated loading, Eng Struct 143 (2017) 441–454. https://doi.org/10.1016/j.engstruct.2017.04.031.

[41] 318-19 Building Code Requirements for Structural Concrete and Commentary, American Concrete Institute, 2019. https://doi.org/10.14359/51716937.

[42] Z. 'Nanni, A. 'Hussain, Strut-and-Tie Method for GFRP-RC Depp Members, International Journal of Concrete Materials and Structures (n.d.).

[43] C.S.A. (Canadian S. Association), Design and construction of building structures with fibre-reinforced polymers, CAN/CSA S806-12 (2012).

[44] S.S.M.M.S.C.N.A. Mojabi, Coastal Protection with FRP-Wrapped Concrete Elements, Engineering (n.d.).

[45] Standard Test Method for Density of Liquid Coatings, Inks, and Related Products 1, (n.d.). https://doi.org/10.1520/D1475-13R20.

[46] Standard Test Method for Tensile Properties of Glass Fiber Strands, Yarns, and Rovings Used in Reinforced Plastics 1, (n.d.). https://doi.org/10.1520/D2343-17.

[47] Eurocode 2: Design of Concrete Structures-Part 1: General rules and rules for buildings, n.d. www.communities.gov.uk.

[48] H.G. Harris, G. Sabnis, Structural modeling and experimental techniques, CRC press, 1999.

[49] 318-19 Building Code Requirements for Structural Concrete and Commentary, American Concrete Institute, 2019. https://doi.org/10.14359/51716937.